Earth and Space Science

Key Points:
- We introduce a new system helping decision making for planetary exploration
- We present an in-depth case study for Mars, providing new insights to aid future geological studies and landing site selections
- We quantify the impact of higher landing elevations and higher rover speeds on our ability to explore Mars

Computer-Aided Exploration of the Martian Geology

Guillaume Rongier[1] [ID] and Victor Pankratius[1] [ID]

[1]Datascience in Astro- & Geoinformatics Group, Massachusetts Institute of Technology, Cambridge, MA, USA

Abstract Motivated by growing amounts of data and enhanced resolution from orbiters and rovers, systems for computer-aided decision support are becoming invaluable in planetary exploration. This article illustrates the value of such systems for a case study on the exploration of the Martian geology, along with improvements in assessing the favorability for landing. Under the current technical status quo for landing and rover's mobility, results show that Eastern Margaritifer Terra and Meridiani Planum stand out due to their high density of scientific targets and flat surfaces. However, our approach allows us to scale the analysis using different scenarios for the entire planet, quantifying the substantial benefits should higher landing elevations and higher rover speeds be realized in the future. This analysis offers new insights into the interplay of technical and scientific constraints.

1. Introduction

Increasing data volumes in planetary exploration have facilitated major breakthroughs about Mars. Currently, data from orbiters, landers, and rovers are exceeding the 100 terabits range (NASA's Mars Exploration Program, 2010; Nelson et al., 2001) and have made considerable contributions to our understanding of the planet's past (Carter et al., 2013; Grotzinger et al., 2014; Morris et al., 2010). New perspectives have been opened up since Schiaparelli's canals (Zahnle, 2001), but uncertainties remain about the precise evolution of Mars, the extent of its past and present hydrosphere, and whether life emerged. All of these questions will require additional data acquisition and analysis, and a new generation of tools is needed to improve the creation of scientific insight at various spatial and temporal scales.

The selection of a landing site epitomizes those needs: in situ exploration of Mars is essential to answer open questions (E2E-iSAG, 2012). However, it is a difficult optimization task with many — possibly conflicting — objectives, which implies subjective choices based on expert judgment and takes several years of planning (Golombek et al., 2012, 2015). So far, more systematic approaches for site selection (Blair et al., 2016; Ono et al., 2016; Oosthoek et al., 2015) that involve decision support or artificial intelligence techniques have received little attention. Also, scant attention has been devoted to planet-wide scenario analyses to derive the impact of mission objectives and engineering capabilities on future explorations.

This article presents a method to predict potential traverse paths an explorer might follow to visit some scientific targets and to leverage such information in a favorability that quantifies the suitability of a site for landing. To our knowledge, this is the first planet-wide study that attempts to quantify our ability to explore Mars in a systematic and optimal fashion that includes technical and scientific constraints. We consider a mission similar to National Aeronautics and Space Administration (NASA)'s Mars 2020 rover, where engineering constraints aim for horizontal, even, and dust-free areas at low elevation in equatorial regions. Scientifically, the mission focuses on visiting an ancient habitable site with magmatic outcrops nearby, to gain better insight on the evolution of Mars (Golombek et al., 2015).

2. Methods

Our work relies on two key methods for landing site selection: (i) fuzzy logic, to fuse spatial data sets depending on exploration constraints; (ii) the fast marching method, to emulate an explorer's traverse path toward the scientific targets after landing.

2.1. Building Favorability Maps With Fuzzy Logic

Fuzzy logic (Zadeh, 1965) states that a proposition is not just false or true, 0 or 1, but that its truthfulness can range anywhere between 0 and 1. It has already been suggested as a method to assess terrain safety during
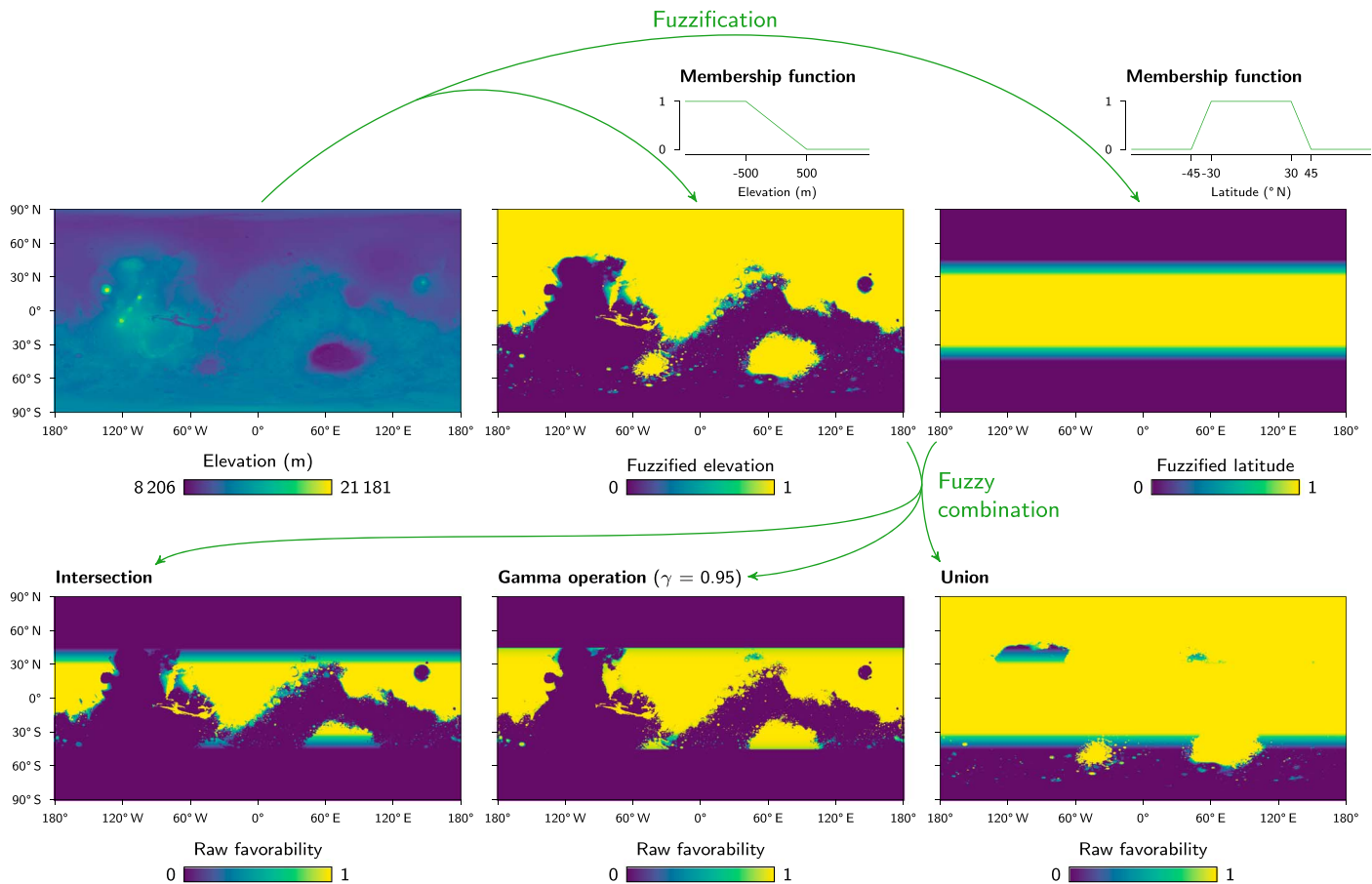
Figure 1. Raw favorability mapping using fuzzy logic and the MOLA elevation at 32 pixels per degree. The fuzzification applies membership functions to the data to define favorable and unfavorable areas for selection. The fuzzy combination gathers all the fuzzified data into a single raw favorability map. MOLA = Mars Orbiter Laser Altimeter.

descent (Howard & Seraji, 2002; Serrano & Seraji, 2007), but has been more widely used in geosciences to map favorable areas by combining raster data (e.g., An et al., 1991; Bingham et al., 2012; Gemitzi et al., 2006; Lee, 2007). It applies naturally to site selection. For instance, a low landing elevation implies a denser atmosphere, which better slows down the descent. But the atmosphere density also depends on uncertain meteorological conditions. Thus, this uncertainty should translate into a range of increasing elevations that become less and less favorable, rather than a strict elevation limit above which the landing becomes impossible.

We leverage fuzzy logic using planetary data converted into raster maps. These data are processed in two steps (Figure 1):

1. The fuzzification uses membership functions to scale the maps between 0 and 1. A site with a fuzzified value equal to 1 is highly favorable for selection; conversely, a fuzzified value of 0 is highly unfavorable.
2. The fuzzy combination uses element-wise operators to combine all the fuzzified data into a single raw favorability map.

Any function that maps input values to the range [0, 1] can be used as membership function. The following fuzzy operators process or combine raster data (Figure 1): complement, intersection, union, gamma operation, algebraic sum, and algebraic product. The complement corresponds to the *not* operation:

$$\mu_c = 1 - \mu \tag{1}$$

where μ is the value of a fuzzified data set at a given cell, and μ_c is the value for that cell. The intersection corresponds to the *and* operation:

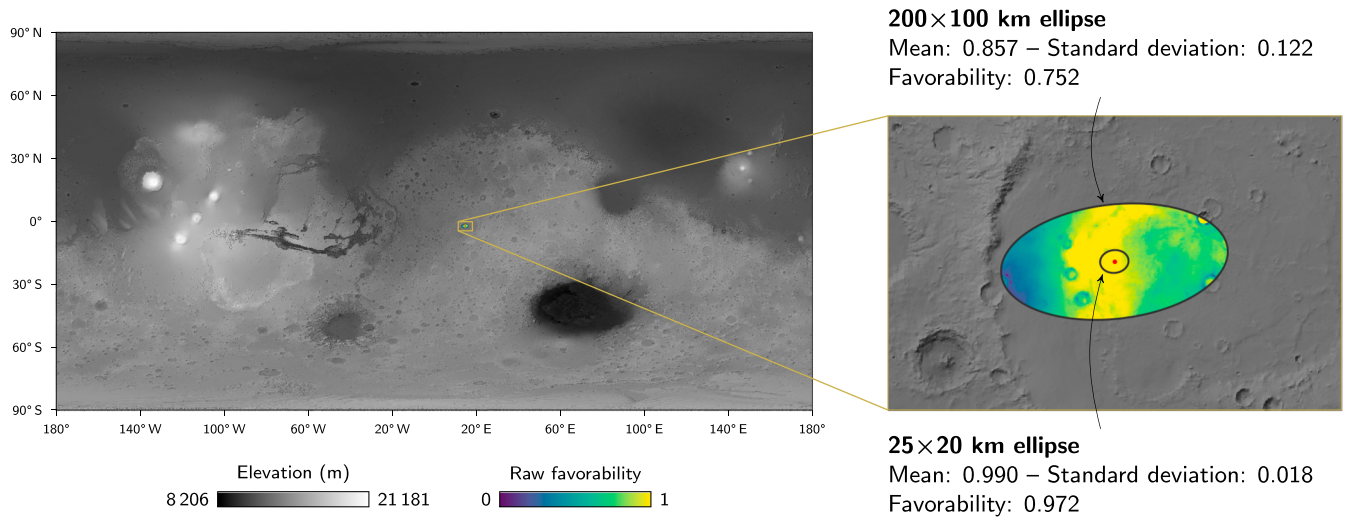$$\mu_c = \min(\mu_1, \ldots, \mu_n) \tag{2}$$

Figure 2. Favorability computation from the raw favorability, based on the MOLA elevation at 128 pixels per degree. The favorability is the algebraic product between the average raw favorability inside the ellipse and the complement of the standard deviation; 200×100 km corresponds to Pathfinder's ellipse size; 25×20 km to Curiosity's ellipse size. MOLA = Mars Orbiter Laser Altimeter.

where μ_i is the value of the fuzzified data set i at a given cell, and μ_c is the combined fuzzified value for that cell. The union corresponds to the *or* operation:

$$\mu_c = \max(\mu_1, \ldots, \mu_n) \tag{3}$$

The gamma operation is a more flexible operation:

$$\mu_c = \left(1 - \prod_{i=1}^{n}\left(1 - \mu_i\right)\right)^{\gamma}\left(\prod_{i=1}^{n}\left(\mu_i\right)\right)^{1-\gamma} \tag{4}$$

When $\gamma = 1$, the gamma operator turns into the algebraic sum; when $\gamma = 0$, the gamma operator turns into the algebraic product. The algebraic sum is an increasing operator, because its result is always higher than the maximum value and, thus, higher than the union. The algebraic product is a decreasing operator, because its result is always lower than the minimum value and, thus, lower than the intersection. They both take into account all the values of the input data in the combined value, contrary to the intersection and union. The gamma operator allows an adjustment between the algebraic sum and product, thus providing a weighted result (Figure 1).

Once all the data have been combined into a raw favorability map, a last step takes into account various uncertainties of the landing location. The uncertainties come from trajectory variations and potential navigation errors during descent. A landing ellipse specifies where the rover will most likely land, considering these uncertainties. The ellipse should be as small as possible, for safety and also for scientific reasons, because it allows a landing as close as possible to the first scientific target to visit. We model this uncertainty by computing the mean and the standard deviation of the raw favorability inside an elliptical neighborhood for each cell of the map (Figure 2). A weighted mean could express the higher probability of landing near the center of the ellipse, although this approach has not been used in our analysis. The final favorability results from the algebraic product between the mean and the complement of the standard deviation, in order to take into account the heterogeneity of the raw favorability inside the ellipse.

2.2. Emulating Explorer Mobility With the Fast Marching Method

The majority of scientific targets are represented as vector data mostly derived from remotely sensed data. Computing a Haversine distance field from the vector data would represent a simple solution to consider the explorer's mobility and to convert those data into raster maps, as required by fuzzy logic. However, such an approach would not take into account whether a terrain is traversable. We use instead the fast marching method (Sethian, 1996, 1999) to emulate the rover's mobility based on terrain-dependent speeds. Starting
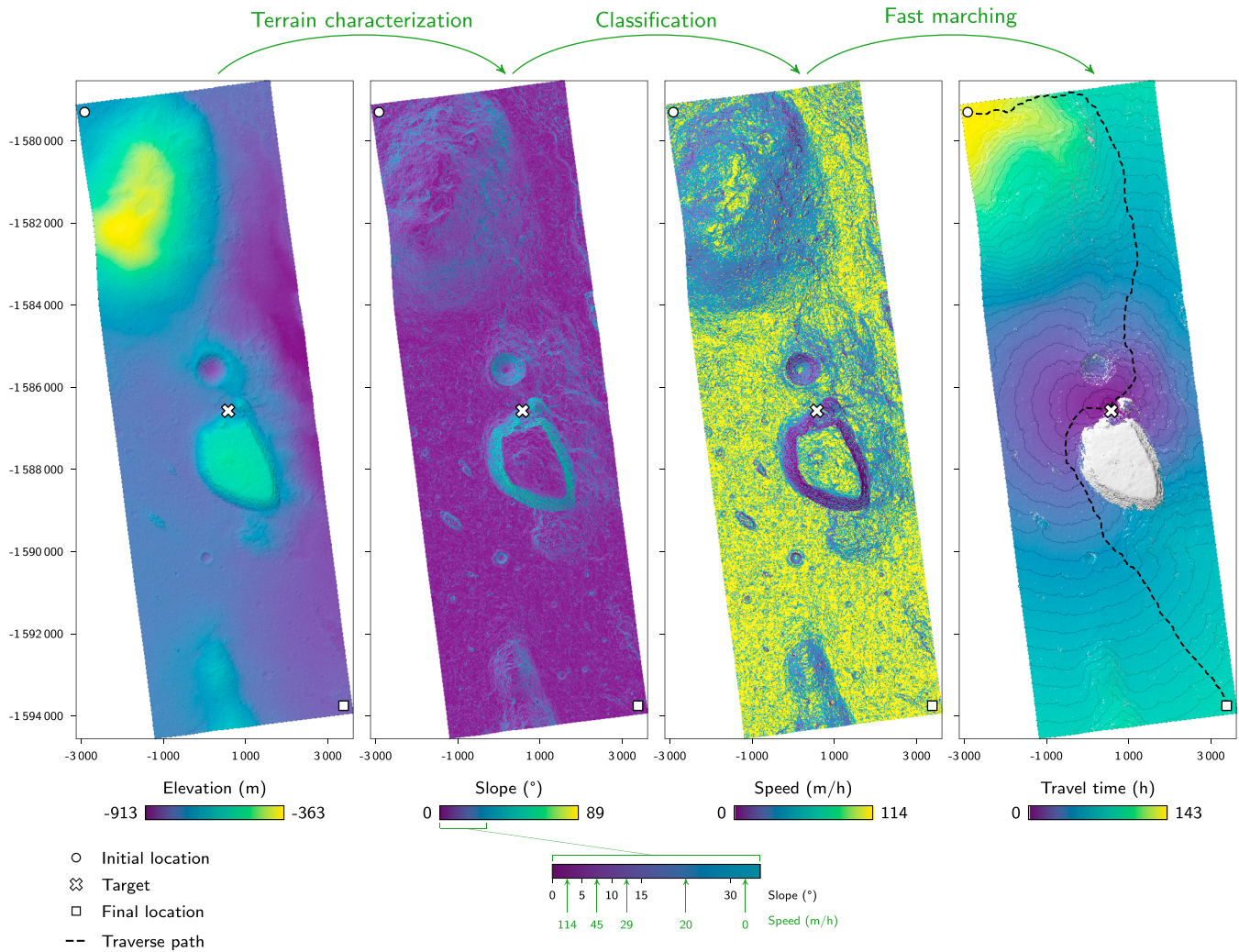
Figure 3. Fast marching used for travel time estimation, based on the HiRISE digital elevation model DTEED_029815_1530_030092_1530_A01. The front propagation starts from one or several targets at the same time. The traverse path comes from a back propagation from the initial and final locations of the rover to the target, which propagates cell by cell by selecting the cell in the neighborhood with the lowest time value. Back propagation is simple but imprecise, and more elaborate methods (e.g., Kimmel et al., 1995) need to be considered for purposes other than visualization. HiRISE = High-Resolution Imaging Science Experiment.

from one or several initial locations, the fast marching propagates a front, and for each cell it computes the arrival time T of the front by solving the Eikonal equation:

$$|\nabla T|F = 1 \tag{5}$$

It requires only the velocity F at which the explorer can go for every cell. The idea is to compute the travel time from each cell in the study area to the closest scientific target (Figure 3). Rovers such as Curiosity must switch driving modes depending on terrain accessibility (Golombek et al., 2012). Some modes require the rover to regularly stop and check its surroundings for high slopes or potential obstacles, such as dust or rocks, slowing it down. Thus, a map of rover speed must be created based on the terrain characteristics on which each mode will be used.

Fuzzifying and combining the travel time maps for each type of scientific targets can quickly incorporate those targets into the overall favorability assessment. However, it may lead to inappropriate results (Figure 4). An intersection produces a map with the highest favorability in between two targets, but this would be the worst possible location to visit both targets. Instead, a landing site as close as possible to one of the targets should be favored. A union produces the corresponding configuration; however, it has a large favorable area around
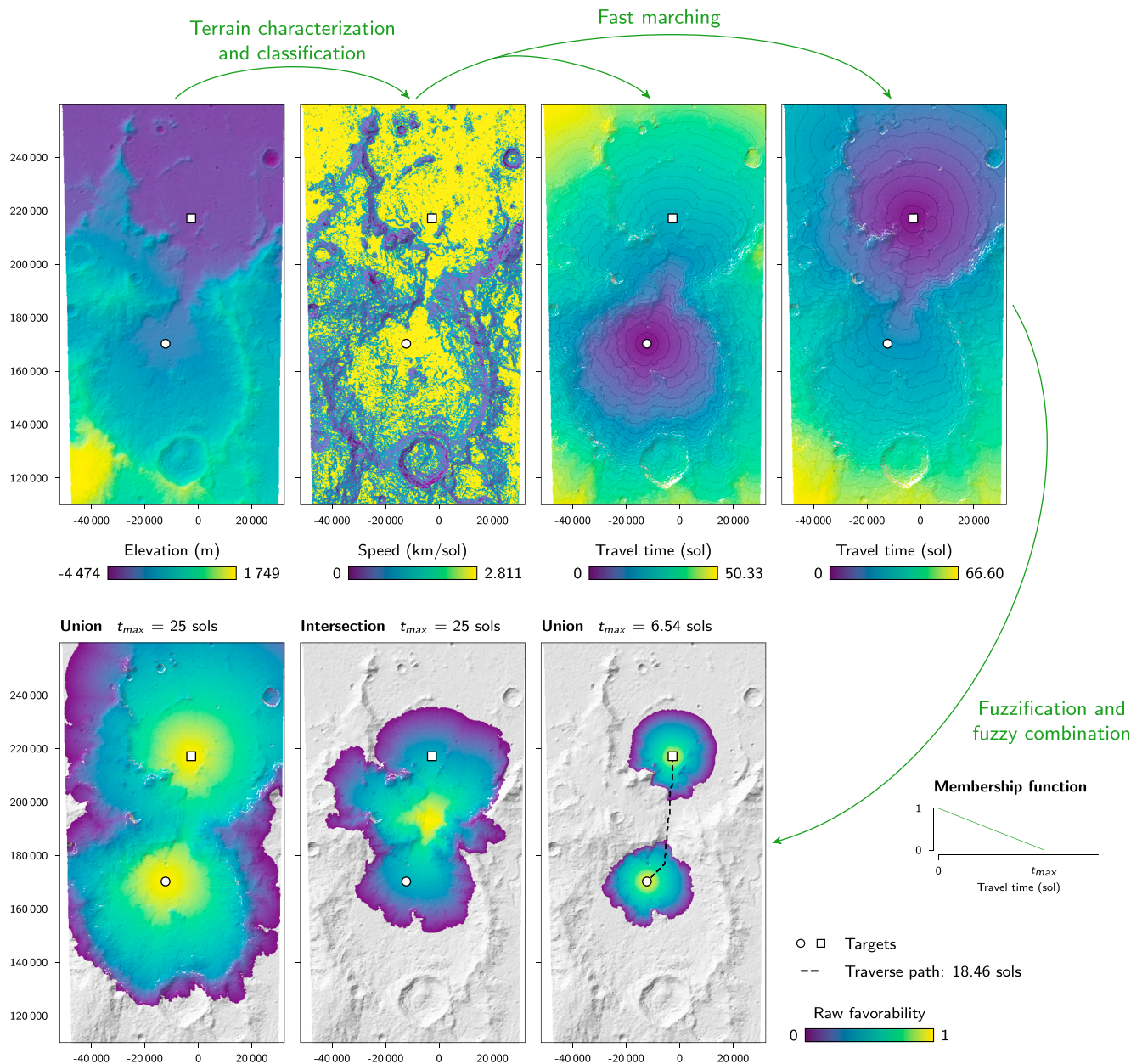
Figure 4. Integration of the fast marching in the fuzzy logic, based on the HRSC digital elevation model H2162_0002. The front propagation is carried out from one or several locations of interest. The total driving time for the mission is set to 25 sols; this results in 6.54 sols available to reach the first target, given the requirement that the second target must be reached as well. HRSC = High-Resolution Stereo Camera.

the targets as a side effect, meaning that the second target may not be visited in time. In addition, not all targets are deemed equal depending on mission objectives.

Targets must be grouped and prioritized depending on those objectives. Grouping gathers the targets that share similar characteristics and are considered interchangeable. It helps to manage the targets with few data points, which otherwise could lead to a widespread low favorability. The prioritization separates the high-priority groups of targets, which must all be visited during the prime mission, from other targets of opportunity. Grouping and prioritizing leverage travel time maps to enhance the favorability values on the most relevant areas according to the mission. Those maps reveal which targets are reachable from a given target. A target is reachable if it is located at a distance that can be reached in less than the total driving time allotted to the mission.

Once we have defined the reachable neighbors of each target, we can select the targets whose neighborhood includes a target from each high-priority group. We call these targets *threshold targets* and compute a new travel time map for them. Including this map in the fuzzy logic highlights the areas of scientific interest for further study. Thanks to the prioritization, it is a more elaborate form of union: it focuses on the areas where the scientific objectives could be met; however, it does not check whether all the high-priority targets in the neighborhood could actually be visited during the prime mission.

To consider that constraint, we compute the traverse paths starting from the threshold targets and then traveling from target to target until the driving time allotted to the mission is reached. Some paths do not visit a target from each high-priority group and are eliminated. In the remaining paths, some may arise from the same initial target. In this case, we rank them and keep only the best one. The rank *r* for a path is based on five components:

$$r = \sum_{i=0}^{N_p} \left(\omega_{\text{ug},i} \frac{n_{\text{ug},i}}{N_{g,i}} \right) + \omega_g \sum_{i=0}^{N_p} \left(1 - \frac{n_{\text{ug},i}}{n_{g,i}} \right) + \omega_d \frac{d_s}{d} + \omega_t \left(1 - \frac{t}{t_{\max}} \right) + \omega_h \frac{\sum_{i=0}^{n} n_h}{N_h n} \tag{6}$$

Each component lies between 0 and 1, with 1 being the best score.

The first component checks whether each target group from each priority level appears in the path: N_p is the number of priority levels; $n_{\text{ug},i}$ is the number of unique groups in the path for a level *i*; $N_{g,i}$ is the total number of groups for a level *i*; and $\omega_{\text{ug},i}$ is the weight of the component, which can vary for each priority level. The second component looks for the number of groups at each priority level: $n_{g,i}$ is the number of groups in the path for a level *i*, and ω_g is the weight of the component. The third component measures the path's sinuosity: *d* is the length of the path, d_s is the straight distance between the initial and final target, and ω_d is the weight of the component. The fourth component looks for the remaining time after reaching all the high-priority groups (but not necessarily all the path's targets): *t* is the time to reach every high-priority group, $t_{\max}$ is the maximum traverse time allowed, and ω_t is the weight of the component. Finally, the fifth component looks for the number of high-resolution data points available along the path: *n* is the number of targets of the path, n_h is the number of high-resolution data available at a target, N_h is the number of high-resolution data, and ω_h is the weight of the component.

Then, for each path, a membership function fuzzifies the travel time from the path's initial target. The fuzzification is based on the remaining time from the mission's allotted driving time after reaching all the high-priority groups (Figure 4). The final fuzzified map is the union of all the fuzzified travel times for each initial target and is used in the fuzzy logic.

Because the fast marching method is a numerical algorithm, inaccuracies can accumulate and travel time can be different when driving from one target to another or the other way around. To account for this aspect in determining the threshold targets and traverse paths, we gather all the travel times between two locations from all the maps, going both ways. Here we choose to use the maximum value as travel time between the targets at those locations, to explore worst-case scenarios.

3. Data and Processing Workflow

Orbital data and their interpretation constitute the basis of our work, which processes them into a favorability map for site selection. This workflow was implemented in Python within Jupyter notebooks (Thomas et al., 2016; the notebooks are available at github.com/MITHaystack/science-casestudies/tree/master/planetary/mars_exploration), using Geospatial Data Abstraction Library/OGR (GDAL Development Team, 2015) to access the data, NumPy (Walt et al., 2011) to operate on the data, and Matplotlib (Hunter, 2007) to visualize the results.

3.1. Data Types and Sources

Engineering constraints (see supporting information, Table S1) rely on three main features: latitude, Mars Orbiter Laser Altimeter elevation (Smith et al., 2003) from NASA's Planetary Data System Geosciences Node and its derivatives such as Horn's slope (Horn, 1981), and thermophysical units (Putzig, 2006). They aim to assess the climatic conditions and terrain characteristics most favorable for the rover and are the only raster maps in our data set. Thus, the constraint with the lowest resolution defines the resolution of the final favorability map, and all the other constraints should be converted to the same resolution. Here the lowest resolution

is 20 pixels per degree, from the thermophysical units. We do not use other constraints such as the rock abundance, because their low resolution (8 pixels or fewer per degree) makes it harder to characterize the favorability and its variations inside the landing ellipse.

Twenty pixels per degree is equivalent to 3-km-wide cells along the equator, in which many details are lost. The footprints of high-resolution data from NASA's Planetary Data System Geosciences Node (Table S1) somewhat counterbalance this loss, by indicating the areas where local studies are possible. High-Resolution Imaging Science Experiment (HiRISE) Digital Elevation Models (DTM) and High-Resolution Stereo Camera (HRSC) DTM map the elevation at 1–2 m/pixel and 25–200 m/pixel, respectively. Compact Reconnaissance Imaging Spectrometer for Mars (CRISM) Full Resolution Targeted (FRT) measures provide spectral data at 18 m/pixel. HiRISE Reduced Data Records (RDR) provide terrain images at 0.25–0.5 m/pixel. All those data can help to better characterize the terrain properties (e.g., Golombek et al., 2012). Other data that can be considered high resolution, such as Context Camera (CTX) terrain images or Thermal Emission Imaging System (THEMIS) spectral data, were not used, because they already cover most—if not all—of Mars. Footprints are vector data, which do not have restriction of resolution.

The scientific targets (see supporting information, Table S2) are also vector data. The vast majority of them come from orbiters; some come from landers and rovers. They contain various geological units and structures from sedimentary, volcanic, tectonic, and impact origin gathered from the United States Geological Survey maps of Mars (Tanaka et al., 2005, 2014), the NASA/International Cartographic Association (ICA) Integrated Database of Planetary Features (Hargitai, 2016; more information on the data and their authors can be found at planetarydatabase.wordpress.com), the NASA Mars Crater Database (Robbins & Hynek, 2012), and individual sources (Bleacher et al., 2007, 2009; Carter et al., 2013; Dohm et al., 2000; Ehlmann & Edwards, 2014; Farmer, 1996; Hauber et al., 2013; Hynek et al., 2010; Irwin & Grant, 2009; Malin & Edgett, 2000; Malin et al., 2010; Marzo et al., 2010; Metz et al., 2009; Osterloo et al., 2010; Richardson et al., 2013). Among these sites, the geological units do not necessarily contain any interesting targets, because some correspond to a mixture of undifferentiated rocks at the considered resolution and others stand in dusty areas. Using geological units directly as targets adds numerous cells to the analysis, because they cover large areas and makes the processing more time consuming. Thus, we intersect them with all the other scientific targets before using them in the fast marching algorithm. This step restrains the selection process to the areas where actual targets have already been interpreted and where we could find other targets that fit the mission's objectives.

3.2. Exploration Scenarios

Our case study exemplifies four possible exploration scenarios (see supporting information, Table S2). The first two scenarios focus on the objectives of the Mars 2020 mission. Scenario A considers potential past standing water environments—for example, lakes and related deposits such as deltaic deposits—on Early to Middle Noachian units as high-priority targets. Such environments are probably the most favorable for the emergence and preservation of life (Summons et al., 2011). Scenario B focuses on similar standing water environments, but located near the Noachian-Hesperian boundary. These environments are comparable to those explored by Curiosity, whose past habitability has been documented (Grotzinger et al., 2014), even though no evidence of past life has yet been found. This scenario should allow further studies of the debated change from a wetter Mars to the current dry climate (Ehlmann et al., 2011; Hynek et al., 2010; Wordsworth, 2016).

The final two scenarios explore some alternatives. Scenario C prioritizes potential past groundwater environments—possibly accessible through deep craters—which may have been more favorable to life than the surface (Michalski et al., 2013). Scenario D focuses on the spatial association of water- and magma-related features, mainly because absolute geochronology on in-place magmatic rocks would tremendously improve current models of Martian chronology (E2E-iSAG, 2012).

3.3. Workflow for Favorability Map Computation

The values for the fuzzification (Figure 5) are based on the Mars 2020 rover specifications (Mustard et al., 2013), which remain similar to those of Curiosity (MSL Project, 2007). The Mars 2020 rover is not expected to drive more than 25 km. Considering that Curiosity has driven at an average speed of 40 m/hr, this is almost equivalent to driving continuously for 25 Martian days or sols (a sol corresponds to 24 h 39), which is set as the maximum driving time for our study. The ellipse to derive the favorability from the raw favorability is 25 × 20-km wide and oriented east-west. Narrower landing ellipses are aimed for the Mars 2020 rover, but we use the largest ellipse to explore the worst-case scenario in terms of landing uncertainty. The weights for the
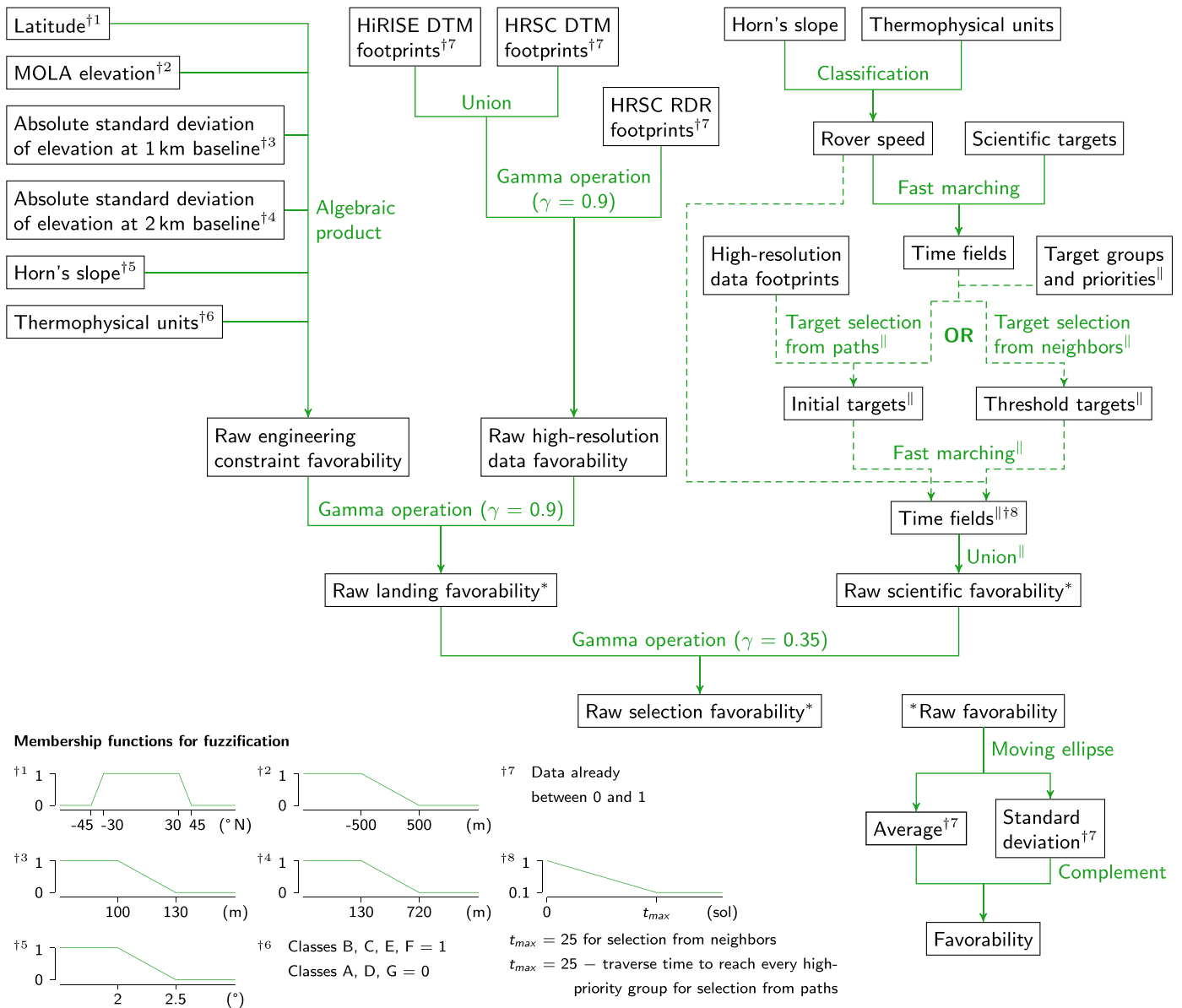
Figure 5. Workflow for the computation of the selection favorability. The dagger † symbolizes fuzzified data. Parallel bar $^\parallel$ denotes duplicated steps in multiple exploration scenarios, defined by different grouping and prioritization of scientific targets. A union operator gathers all the scenarios into a single raw scientific favorability map; however, the favorability map computed in each scenario could be used individually as well. The asterisk * denotes maps that are converted from a raw favorability to a favorability that takes the region of the landing ellipse into account. During fuzzification, the default value for a cell with no data is 0. The high-resolution data footprints correspond to the HiRISE DTM and RDR, the HRSC DTM, and the CRISM FRT footprints. HiRISE = High-Resolution Imaging Science Experiment; DTM = Digital Elevation Model; RDR = Reduced Data Records; DTM = Digital Elevation Model; CRISM = Compact Reconnaissance Imaging Spectrometer for Mars; FRT = Full Resolution Targeted.

path's ranks become $\omega_{ug,i} = i + 1$, $\omega_g = 1$, $\omega_d = 0.5$, $\omega_t = 0.5$, $\omega_h = 0.5$, and remain the same in each exploration scenario. They emphasize keeping the paths that visit more target groups, especially those with the highest priority.

The fast marching requires a map for the rover speed on the entire planet (see supporting information, Figure S1). This map comes from the classification of Horn's slope (Horn, 1981) and thermophysical units (Putzig, 2006) to attribute a speed to each cell depending on the terrain characteristics and the driving modes of the rover (Golombek et al., 2012; see supporting information, Tables S4 and S5). The slope can never be higher than 30°, and the speed decreases when the slope increases. Concerning the thermophysical units, classes A, D, and G are dominated by dust, potentially as a thick layer, making them most likely untraversable by the rover. Classes B, E, and F are dominated by sand, rocks, bedrocks, and duricrust, and should be mostly
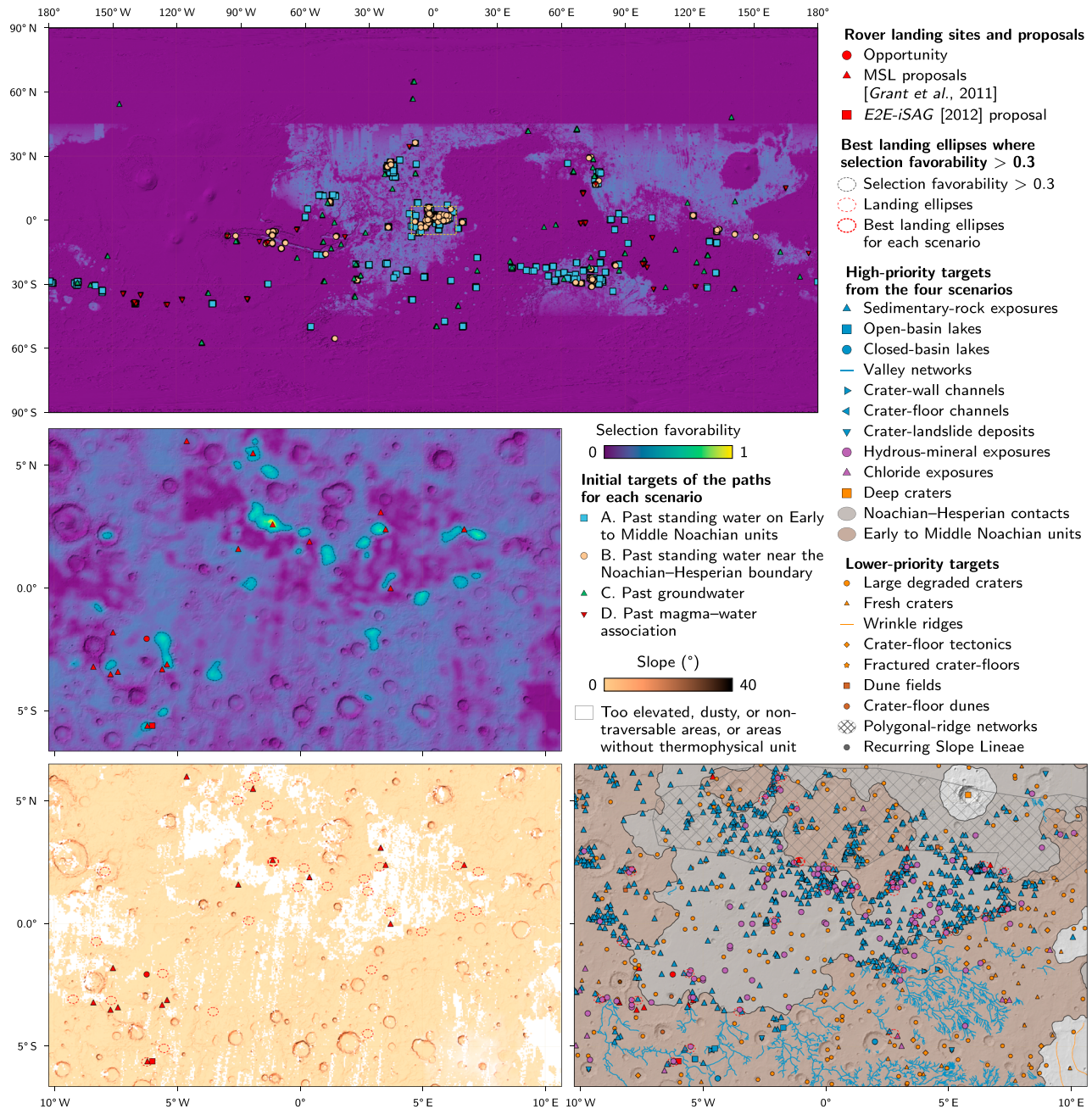
Figure 6. Selection favorability on Mars at 20 pixels per degree with the initial targets of the traverse paths overlaid on a MOLA hillshade, and enlargement on Eastern Margaritifer Terra and Meridiani Planum. The selection favorability includes the four exploration scenarios. MOLA = Mars Orbiter Laser Altimeter.

traversable. Class C stretches between A and B, with some dust and fine sand, which can cause problems. We keep it traversable, but further limit the speed when the slope increases.

Based on these elements, we compute three favorability maps (Figure 5):

- A landing favorability map based on combining the engineering constraints for landing with the footprints of high-resolution data.
- A scientific favorability map based on the time left after visiting all the high-priority targets within the paths, obtained by fast marching. Each scenario has its own scientific favorability maps, which are combined into a single map.
- A selection favorability map based on the combination of the two previous maps.

A. Past standing water on Early to Middle Noachian units

2 151 paths, 7.64$^{22}_{3}$ targets/path
Traverse time (sols): 21.17$^{25}_{2.67}$
Threshold time (sols): 19.29$^{25}_{0}$
Landing favorability: 0.32$^{0.99}_{0}$

Early to Middle Noa. units	6 310
Polygonal-ridge networks	2 716
Sedimentary-rock exposures	1 902
Hydrous-mineral exposures	1 872
Valley networks	1 406
Large degraded craters	449
Chloride exposures	423
Open-basin lakes	271
Crater-wall channels	153
Crater-floor valley deposits	130
Outflow channels	124
Graben axes	90
Deltaic deposits	89
Young deltas	85
Closed-basin lakes	62
Hes. to Am. volcanic units	58
Wrinkle ridges	43
Crater-floor channels	43
Glacial features	36
Channels (not valleys)	30
Dune fields	23
Fractured crater-floors	19
Dissected mantle	17
Gullies	16
Crater-floor tectonics	15
Crater-floor landslide deposits	15
Carbonate exposures	14
Crater-floor dunes	8
Fresh craters	5
Scarps	3
Ridges	2
Deep craters	2
Recurring Slope Lineae	1

B. Past standing water near the Noachian–Hesperian boundary

1 404 paths, 7.26$^{23}_{3}$ targets/path
Traverse time (sols): 20.8$^{25}_{0}$
Threshold time (sols): 18.24$^{25}_{0}$
Landing favorability: 0.36$^{0.99}_{0}$

Noa.–Hes. contacts	3 489
Polygonal-ridge networks	2 569
Sedimentary-rock exposures	1 611
Hydrous-mineral exposures	1 355
Valley networks	454
Chloride exposures	128
Hes. to Am. volcanic units	89
Dune fields	70
Crater-wall channels	63
Large degraded craters	58
Deltaic deposits	57
Young deltas	56
Crater-floor valley deposits	46
Open-basin lakes	39
Graben axes	25
Gullies	21
Crater-floor channels	21
Wrinkle ridges	12
Closed-basin lakes	9
Fractured crater-floors	8
Dissected mantle	7
Crater-floor dunes	5
Scarps	3
Subaqueous fans	2
Fresh craters	1

C. Past groundwater

358 paths, 5.03$^{7}_{2}$ targets/path
Traverse time (sols): 18.39$^{24.92}_{0}$
Threshold time (sols): 17.23$^{24.92}_{0}$
Landing favorability: 0.19$^{0.74}_{0}$

Dune fields	375
Hydrous-mineral exposures	359
Deep craters	358
Crater-floor dunes	252
Large degraded craters	200
Glacial features	62
Gullies	56
Closed-basin lakes	29
Polygonal-ridge networks	20
Sedimentary-rock exposures	16
Crater-floor tectonics	14
Glacier-like forms	12
Crater-floor landslide deposits	10
Fresh craters	8
Hes. to Am. volcanic units	7
Fractured crater-floors	6
Recurring Slope Lineae	4
Crater-floor channels	4
Crevassed glacier-like forms	3
Valley networks	2
Wrinkle ridges	1
Glaciofluvial valleys	1

D. Past water–magma association

1058 paths, 6.33$^{14}_{3}$ targets/path
Traverse time (sols): 21.46$^{25}_{0}$
Threshold time (sols): 19$^{25}_{0}$
Landing favorability: 0.01$^{0.46}_{0}$

Volcanoes	1 673
Valley networks	1 559
Hes. to Am. volcanic units	1 464
Hydrous-mineral exposures	795
Chloride exposures	629
Noa. volcanic units	281
Ridges	66
Dissected mantle	48
Sedimentary-rock exposures	43
Large degraded craters	42
Scarps	33
Channels (not valleys)	16
Crater-wall channels	13
Glaciofluvial valleys	11
Glacial features	10
Wrinkle ridges	8
Fresh craters	5
Graben axes	1

Figure 7. Distributions of scientific targets from the traverse paths of each exploration scenario. Statistical measures are represented as mean$^{max}_{min}$ from all the paths. The traverse time corresponds to the total duration of a path; the threshold time is the duration after having visited all the high-priority targets. The landing favorability (see supporting information, Figure S2) is taken at the location of the initial targets of the paths. Abbreviation: Noa. = Noachian; Hes. = Hesperian; Am. = Amazonian.

The main idea behind the fuzzy combination is to increase the value of areas where all the constraints are met, rather than labeling areas where conditions are partially satisfied as completely unfavorable. For instance, when combining the raw favorability maps for the engineering constraints and the high-resolution data, we want the result to favor the safe areas where high-resolution data are available. But we also want the safe areas without high-resolution data to remain favorable, just slightly less so. Thus, we use a gamma operator with a high gamma value. On the other hand, when combining the resulting raw landing favorability with the raw scientific favorability, we want the safe areas with close scientific targets to stand out. A small gamma value lets the safe areas without close scientific targets remain visible, but they remain far less favorable than those with scientific targets.

4. Results

We have applied our workflow to compute the favorability maps of Mars for landing, exploration, and site selection at 20 pixels per degree.

4.1. Distribution of Favorable Areas

The resulting selection favorability map (Figure 6) shows the areas fitting the landing constraints (see supporting information, Figure S2), even when traverse paths are absent. These areas cover a third of the surface of Mars, including Xanthe Terra, Chryse Planitia, Margaritifer Terra, Terra Meridiani, Isidis Planitia, Elysium Planitia, and Northern Hellas Planitia. The distribution of traverse paths highlights some areas already targeted
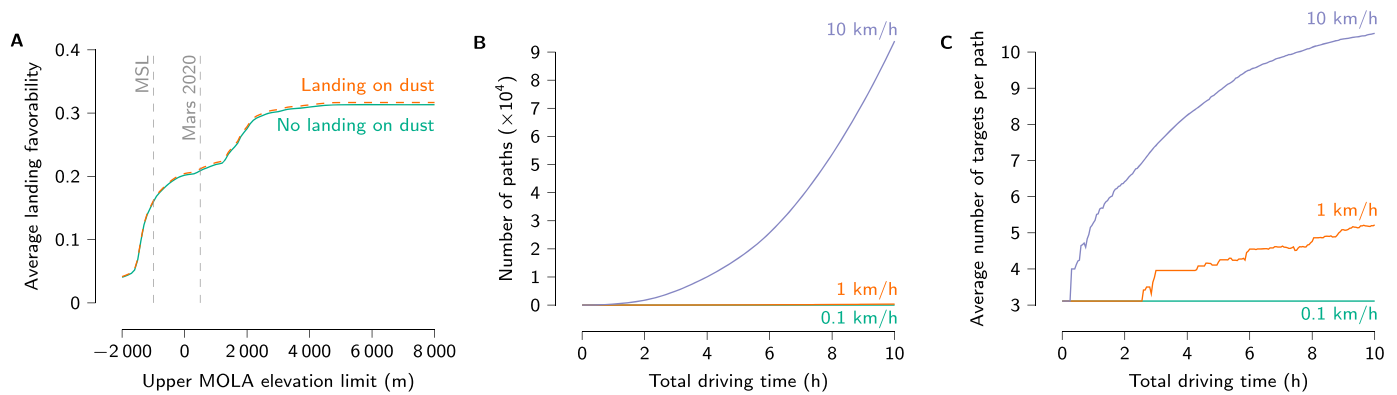
Figure 8. Impact of landing and roving capabilities. (a) Influence of the upper limit for elevation fuzzification on the landing favorability (see supporting information, Figure S2) at the locations of the traverse path's initial targets from all the exploration scenarios. The paths include those on dusty areas. The lower elevation limit is 1 km below the upper limit. MSL is Mars Science Laboratory, Curiosity's program. (b) Influence of the rover speed (see supporting information, Table S5) and total driving time during the mission on the number of traverse paths from all the exploration scenarios. (c) Influence of the rover speed (see supporting information, Table S5) and total driving time during the mission on the number of scientific targets within each traverse path from all the exploration scenarios.

for exploration: Eastern Margaritifer Terra and Meridiani Planum, Xanthe Terra, Mawrth Vallis, Northern Hellas Planitia, Southern Margaritifer Terra, and Northern Syrtis Major Planum (Figure 6). It also highlights other less-renowned areas, especially in the southern part of Mars.

Those paths do not lead to widespread high-favorability areas (Figure 6), because all the targets cannot be reached within 25 sols and even when they can, the remaining driving time may not compensate for the landing uncertainty. Curiosity was not expected to drive more than 20 sols in total during its prime mission (669 sols), and drove for only 9 sols. Using 9 sols, the number of possible paths decreases dramatically: 2151 to 129 for past standing water on Early to Middle Noachian units, 1404 to 108 for past standing water near the Noachian-Hesperian boundary, 358 to 39 for past groundwater, and 1058 to 64 for past water-magma association. Paths' availability even at short driving times could be another criterion for selection, to favor the completion of the mission's main objectives as soon as possible.

Eastern Margaritifer Terra and Meridiani Planum stand out as the only highly favorable areas (Figure 6). This results from a high density of scientific targets, including many hydrous-mineral and sedimentary rock exposures on Early to Middle Noachian terrains or near contacts between Noachian and Hesperian units. Furthermore, this region is mostly flat, which favors a successful landing, unlike other areas with high scientific favorability, such as Mawrth Vallis. Flatness and high target density also allow the rover to go faster and to reach more targets, while providing greater scheduled flexibility to compensate for landing uncertainties. The high favorability is consistent with the numerous proposals targeting those areas and with the rover Opportunity exploring their southwestern part. However, a more local study using data at finer resolution and more recent geological mapping (e.g., Hynek & Di Achille, 2017) would be necessary to comment in more detail on the suitability of the potential landing sites.

4.2. Distribution of Reachable Targets

The traverse paths and scientific targets are unevenly distributed between the four exploration scenarios (Figure 7). The two scenarios related to past standing water seem more promising: they have more targets per path and a far higher landing favorability. Even though we use relaxed priority constraints for the past magma-water association scenario, the number of available paths is limited and they are difficult to reach. These limitations are consistent with a lack of impact-dated magmatic rocks near water-related features. Moreover, the vast majority of the paths rely on valley networks as water-related features, but those networks are not the most promising targets at which to study past habitable environments (Summons et al., 2011).

The scenarios exhibit more similar average traverse times: all come close to 20 sols over the 25 allotted, and all need almost an entire path to reach all the high-priority targets. This result shows how far away targets can be from one another. It implies that long missions are to be expected to fulfill all the objectives with our current capabilities.
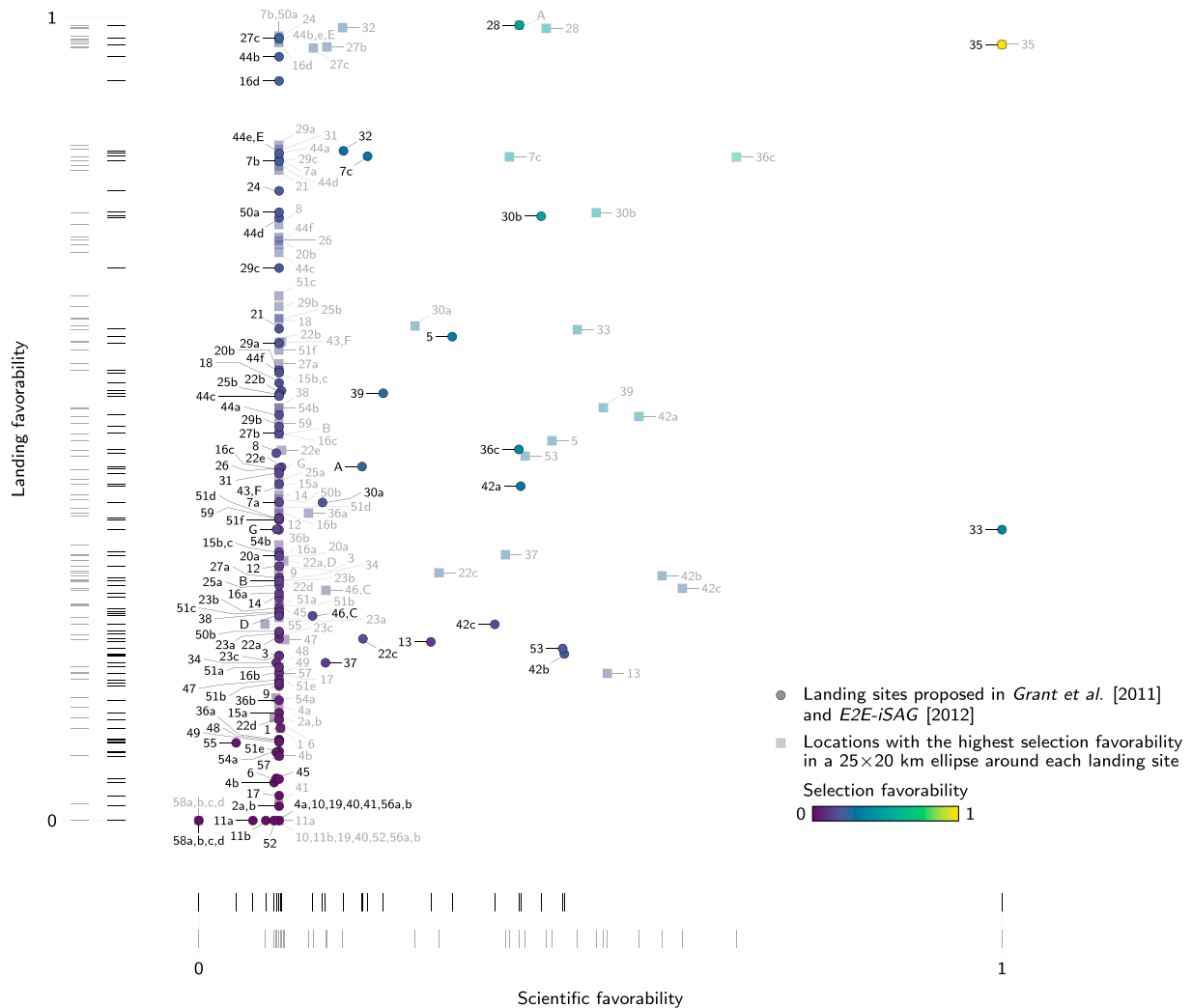
Figure 9. Landing, scientific, and selection favorability from the traverse paths for some landing sites proposed in previous studies (dots) and nearby locations with higher selection favorability (squares). The bars are the projections of the dots (black) and squares (gray) along each axis. The sites labeled with a number were proposed for the Mars Science Laboratory mission (see Table 4 of Grant et al., 2011 for details about the labels). The sites with a capital letter were proposed for a mission similar to Mars 2020 (see Table 9 of E2E-iSAG, 2012 for details about the labels, which follow the order of the table). The most favorable sites (35, 33, 28, and 30b) are all from Eastern Margaritifer Terra and Meridiani Planum.

4.3. Future Capabilities

Among the potential sites highlighted by our approach, many lie on the southern part of Mars (Figure 6), out of reach with our current landing capabilities. Our approach can help assess the impact of the engineering constraints on site accessibility, for instance, when accessibility is reduced due to landing elevation and dust. According to the constraints in our case study, elevation impacts only landing, but dust impacts landing and roving. Thus, we miss some traverse paths in dusty areas and must recompute the paths using similar speeds on dust-free and dusty areas. The average landing favorability from the paths' initial targets quantifies how the targets' accessibility evolves when we loosen the engineering constraints for landing in the fuzzification (Figure 8a). Being able to land on dusty areas does not appreciably increase accessibility, mostly because few targets are located there. However, landing up to 3,000-m high instead of 500 m for the Mars 2020 mission could let us access many new potential landing sites.

Rover mobility also affects the determination of potential landing sites, especially the time allotted to driving and the rover speed. Longer driving times increase the number of targets within a path and the number of paths itself (Figures 8b and 8c). We look at three base speeds from which we recompute the paths (Figures 8b and 8c). At automated-rover speeds (≈0.1 km/hr) such as Curiosity's, the only paths available after 10 hr of traverse are those with colocated high-priority targets. The rover has to drive an extra 15 hr 30 to access new

targets and paths. Increasing to remotely controlled rover speeds ($\approx$1 km/hr) expands the number of paths and targets after about 2 hr 35 only. But the most striking increase comes at human-driven rover speeds ($\approx$10 km/hr), where driving for about 18 min gives access to more paths and targets than reached in an entire sol when traveling at 0.1 km/hr. Thus, rover speed proves to be a decisive factor for increasing the number of explorable targets and for a faster exploration of Mars.

5. Discussion and Perspectives

This work analyzes the current and future opportunities for an exploration of Mars driven by scientific objectives, while considering landing and mobility constraints and the entire planet. It goes one step further than previous studies (Blair et al., 2016; Ono et al., 2016; Oosthoek et al., 2015), which focused on only some of those points. The fuzzy logic plays a major role in this improvement, by fusing all the data into a single, easy-to-read map. The fast marching provides a more precise characterization of the rover's mobility than merely distance (Oosthoek et al., 2015) while being a more natural alternative to the Dijkstra algorithm (Ono et al., 2016). Indeed, it relies directly on the rover speed instead of a cost function and emulates the physical propagation of a front. Thus, its principle is easier to understand for nonspecialists; and the resulting travel time maps are more versatile and easier to analyze. Other methods could integrate ours, especially those based on machine learning for a more exhaustive terrain classification (Jones et al., 2014; Rothrock et al., 2016).

The distribution of hydrous-mineral exposures on the surface of Mars shapes the distribution of the traverse paths. In scenarios regarding past standing water, sedimentary rock exposures also play a major role in establishing the paths, contrary to sedimentary structures identifiable from orbit, such as deltas (Figure 7). However, the exact origin of sedimentary rock exposures is ambiguous, and they are not necessarily an indicator of past standing water. If the preservation of sedimentary structures on Mars is quite extraordinary and attractive, available large-scale data sets that better characterize outcrops' origin and distribution are currently lacking despite their potential importance for exploration. Such analysis is ambitious in terms of workload, and computer-aided tools could also provide substantial support, but this analysis is conceivable using HiRISE data. Similar data sets for magmatic exposures would be a significant advance, because the volcanic units from the geological map of Mars remain too imprecise.

Our analysis highlights how driving time becomes a crucial factor for current missions. Current rovers are slow. They all have stayed viable far beyond their life expectancy, but the travel time to fulfill the multiple objectives should not be neglected, especially in future sampling missions, where timing could become decisive. Such anticipation work can help to better define what could be expected from a rover during the prime mission and its potential extent. It could also help to better plan the driving time required in a given area, and better manage driving versus scientific analysis as these factors compete for time and energy.

On top of areas already widely targeted for exploration, other less-renowned areas stand out in the selection favorability map, such as Ritchey crater, Magong crater, or Kashira carter. Many areas also stand out from the paths, and even if they are not currently accessible, they could guide future studies of orbital data to better assess their ability to fulfill our exploration's objectives. If the benefit of their in situ exploration is confirmed, our approach allows scientists to assess easily at a local scale the engineering characteristics required to go there. Using different exploration scenarios could also highlight other sites as candidate targets.

In any case, local studies are required to better assess favorability, as shown by some previously proposed landing sites (Figure 9): most of those sites have a low scientific favorability, despite their recognized interest. Part of this comes from a lack of precision and completeness of the available data. For instance, lakes are listed as single points, but they could cover a large area, and their interpretation usually relies on several outcrops disseminated over that large area. But a lack of anticipation of landing and traverse conditions in previous studies is another main issue. Here almost all the sites lie near a location with higher selection favorability (Figure 9). Our widespread analysis can guide the identification of the most promising areas for more local study, where the same method can be used to find an optimal landing site more easily.

6. Conclusions

Computer-aided approaches are becoming invaluable in supporting exploration given the growing data volumes and enhanced resolutions in various planetary objects, especially Mars. Our method further contributes to the quest for providing decision support and guidance to scientists and engineers. Its strength comes from

its flexibility, allowing simultaneous, scalable analyses of future what-if scenarios. The comparison of several scientific scenarios highlights the uneven distribution of the explorable targets, with a main role played by hydrous-mineral exposures and a scarcity of magmatic exposures nearby. Technical scenarios show the importance of higher landing elevations and higher rover speeds to further explore Mars. Similar work to help the interpretation of geological features could also be essential, to gather more precise and complete data sets, but also for the same motivation as our work: dealing with the challenging amount of available data. Additionally, the planetary science community can make an invaluable contribution to facilitate automated approaches by making data products of interpretations of geological features openly available in GIS-ready formats.

References

An, P., Moon, W. M., & Rencz, A. (1991). Application of fuzzy set theory to integrated mineral exploration. *Canadian Journal of Exploration Geophysics*, *27*(1), 1–11.

Bingham, L., Zurita-Milla, R., & Escalona, A. (2012). Geographic information system-based fuzzy-logic analysis for petroleum exploration with a case study of northern South America. *AAPG Bulletin*, *96*(11), 2121–2142. https://doi.org/10.1306/04251212009

Blair, D. M., Gowanlock, M., Li, J. D., Rude, C. M., Herring, T., & Pankratius, V. (2016). Improving spacecraft site selection through computer-aided discovery and data fusion. In *47th Lunar and Planetary Science Conference* (pp. 1987). The Woodlands, TX. LPI Contribution No. 1903.

Bleacher, J. E., Glaze, L. S., Greeley, R., Hauber, E., Baloga, S. M., Sakimoto, S. E. H., et al. (2009). Spatial and alignment analyses for a field of small volcanic vents south of Pavonis Mons and implications for the Tharsis province, Mars. *Journal of Volcanology and Geothermal Research*, *185*(1–2), 96–102. https://doi.org/10.1016/j.jvolgeores.2009.04.008

Bleacher, J. E., Greeley, R., Williams, D. A., Cave, S. R., & Neukum, G. (2007). Trends in effusive style at the Tharsis Montes, Mars, and implications for the development of the Tharsis province. *Journal of Geophysical Research*, *112*, E09005. https://doi.org/10.1029/2006JE002873

Carter, J., Poulet, F., Bibring, J.-P., Mangold, N., & Murchie, S. (2013). Hydrous minerals on Mars as seen by the CRISM and OMEGA imaging spectrometers: Updated global view. *Journal of Geophysical Research: Planets*, *118*, 831–858. https://doi.org/10.1029/2012JE004145

Dohm, J. M., Baker, V. R., Anderson, R. C., Scott, D. H., Rice, J. W., & Hare, T. M. (2000). Identifying Martian hydrothermal sites: Geological investigation utilizing multiple datasets. In *31st Lunar and Planetary Science Conference*. Abstract No. 1613, Houston, TX.

E2E-iSAG (2012). Planning for Mars returned sample science: Final Report of the MSR End-to-End International Science Analysis Group (E2e-iSAG). *Astrobiology*, *12*(3), 175–230. https://doi.org/10.1089/ast.2011.0805

Ehlmann, B. L., & Edwards, C. S. (2014). Mineralogy of the Martian surface. *Annual Review of Earth and Planetary Sciences*, *42*(1), 291–315. https://doi.org/10.1146/annurev-earth-060313-055024

Ehlmann, B. L., Mustard, J. F., Murchie, S. L., Bibring, J.-P., Meunier, A., Fraeman, A. A., & Langevin, Y. (2011). Subsurface water and clay mineral formation during the early history of Mars. *Nature*, *479*(7371), 53–60. https://doi.org/10.1038/nature10582

Farmer, J. D. (1996). Hydrothermal systems on Mars: An assessment of present evidence. In G. R. Bock & J. A. Goode (Eds.), *Ciba Foundation Symposium 202—Evolution of hydrothermal ecosystems on Earth (and Mars?)* (pp. 273–303). Chichester, UK: John Wiley. https://doi.org/10.1002/9780470514986.ch15

GDAL Development Team (2015). GDAL - Geospatial Data Abstraction Library: Version 2.0.1.

Gemitzi, A., Petalas, C., Tsihrintzis, V. A., & Pisinaras, V. (2006). Assessment of groundwater vulnerability to pollution: A combination of GIS, fuzzy logic and decision making techniques. *Environmental Geology*, *49*(5), 653–673. https://doi.org/10.1007/s00254-005-0104-1

Golombek, M. P., Grant, J. A., Farley, K. A., & Chen, A. (2015). Science objectives, engineering constraints, and landing sites proposed for the Mars 2020 rover mission. In *46th Lunar and Planetary Science Conference* (pp. 1653). The Woodlands, TX. LPI Contribution No. 1832.

Golombek, M., Grant, J., Kipp, D., Vasavada, A., Kirk, R., Fergason, R., et al. (2012). Selection of the Mars Science Laboratory landing site. *Space Science Reviews*, *170*(1-4), 641–737. https://doi.org/10.1007/s11214-012-9916-y

Grant, J. A., Golombek, M. P., Grotzinger, J. P., Wilson, S. A., Watkins, M. M., Vasavada, A. R., et al. (2011). The science process for selecting the landing site for the 2011 Mars Science Laboratory. *Planetary and Space Science*, *59*(11), 1114–1127. https://doi.org/10.1016/j.pss.2010.06.016

Grotzinger, J. P., Sumner, D. Y., Kah, L. C., Stack, K., Gupta, S., Edgar, L., et al. (2014). A habitable fluvio-lacustrine environment at Yellowknife Bay, Gale crater, Mars. *Science*, *343*(6169), 1242777. https://doi.org/10.1126/science.1242777

Hargitai, H. (2016). Metacatalog of planetary surface features for multicriteria evaluation of surface evolution: The integrated planetary feature database. In *DPS 48/EPSC 11 Meeting #426.23*. Pasadena, CA.

Hauber, E., Platz, T., Reiss, D., Le Deit, L., Kleinhans, M. G., Marra, W. A., et al. (2013). Asynchronous formation of Hesperian and Amazonian-aged deltas on Mars and implications for climate. *Journal of Geophysical Research: Planets*, *118*, 1529–1544. https://doi.org/10.1002/jgre.20107

Horn, B. K. P. (1981). Hill shading and the reflectance map. *Proceedings of the IEEE*, *69*(1), 14–47. https://doi.org/10.1109/PROC.1981.11918

Howard, A., & Seraji, H. (2002). A fuzzy rule-based safety index for landing site risk assessment. In *Proceedings of the 5th Biannual World Automation Congress* (Vol. 14, pp. 579–584). New York: IEEE. https://doi.org/10.1109/WAC.2002.1049499

Hunter, J. D. (2007). Matplotlib: A 2D graphics environment. *Computing in Science Engineering*, *9*(3), 90–95. https://doi.org/10.1109/MCSE.2007.55

Hynek, B. M., Beach, M., & Hoke, M. R. T. (2010). Updated global map of Martian valley networks and implications for climate and hydrologic processes. *Journal of Geophysical Research*, *115*, E09008. https://doi.org/10.1029/2009JE003548

Hynek, B. M., & Di Achille, G. (2017). Geologic map of Meridiani Planum, Mars. In *USGS Numbered Series 3356*. Reston, VA: U.S. Geological Survey. iP-070106.

Irwin, R. P. I., & Grant, J. A. (2009). Large basin overflow floods on Mars. In D. M. Burr, et al. (Eds.), *Megaflooding on Earth and Mars* (pp. 209–224). Cambridge, UK: Cambridge University Press. https://doi.org/10.1017/CBO9780511635632.011

Jones, E., Caprarelli, G., Mills, F. P., Doran, B., & Clarke, J. (2014). An alternative approach to mapping thermophysical units from Martian thermal inertia and albedo data using a combination of unsupervised classification techniques. *Remote Sensing*, *6*(6), 5184–5237. https://doi.org/10.3390/rs6065184

Kimmel, R., Amir, A., & Bruckstein, A. M. (1995). Finding shortest paths on surfaces using level sets propagation. *IEEE Transactions on Pattern Analysis and Machine Intelligence*, *17*(6), 635–640. https://doi.org/10.1109/34.387512

Lee, S. (2007). Application and verification of fuzzy algebraic operators to landslide susceptibility mapping. *Environmental Geology*, *52*(4), 615–623. https://doi.org/10.1007/s00254-006-0491-y

MSL Project (2007). MSL landing site selection user's guide to engineering constraints (Tech. Rep. 4.5). Pasadena, CA: The Mars Science Laboratory Project, Jet Propulsion Laboratory.

Malin, M. C., & Edgett, K. S. (2000). Sedimentary rocks of early Mars. *Science*, *290*(5498), 1927–1937. https://doi.org/10.1126/science.290.5498.1927

Malin, M. C., Edgett, K. S., Cantor, B. A., Caplinger, M. A., Danielson, G. E., Jensen, E. H., et al. (2010). An overview of the 1985–2006 Mars Orbiter Camera science investigation. *The Mars Journal*, *5*, 1–60. https://doi.org/10.1555/mars.2010.0001

Marzo, G. A., Davila, A. F., Tornabene, L. L., Dohm, J. M., Fairén, A. G., Gross, C., et al. (2010). Evidence for Hesperian impact-induced hydrothermalism on Mars. *Icarus*, *208*(2), 667–683. https://doi.org/10.1016/j.icarus.2010.03.013

Metz, J. M., Grotzinger, J. P., Mohrig, D., Milliken, R., Prather, B., Pirmez, C., et al. (2009). Sublacustrine depositional fans in southwest Melas Chasma. *Journal of Geophysical Research*, *114*, E10002. https://doi.org/10.1029/2009JE003365

Michalski, J. R., Cuadros, J., Niles, P. B., Parnell, J., Deanne Rogers, A., & Wright, S. P. (2013). Groundwater activity on Mars and implications for a deep biosphere. *Nature Geoscience*, *6*(2), 133–138. https://doi.org/10.1038/ngeo1706

Morris, R. V., Ruff, S. W., Gellert, R., Ming, D. W., Arvidson, R. E., Clark, B. C., et al. (2010). Identification of carbonate-rich outcrops on Mars by the Spirit Rover. *Science*, *329*(5990), 421–424. https://doi.org/10.1126/science.1189667

Mustard, J. F., Adler, M., Allwood, A., Bass, D. S., Beaty, D. W., Bell, J. F., et al. (2013). Report of the Mars 2020 Science Definition Team (Tech. Rep). Mars Exploration Program Analysis Group (MEPAG).

NASA's Mars Exploration Program (2010). NASA Mars Orbiter Speeds Past Data Milestone.

Nelson, S. V., Arvidson, R. E., Slavney, S., & Springer, R. J. (2001). Mars Exploration Program: Expected data volumes and data access requirements for research and public engagement (Tech. Rep. Draft 2.0). St. Louis, MO/Pasadena, CA: Washington University/Jet Propulsion Laboratory.

Ono, M., Rothrock, B., Almeida, E., Ansar, A., Otero, R., Huertas, A., & Heverly, M. (2016). Data-driven surface traversability analysis for Mars 2020 landing site selection. In *2016 IEEE Aerospace Conference* (pp. 1–12). https://doi.org/10.1109/AERO.2016.7500597

Oosthoek, J. H. P., Arriazu, P., & Marco Figuera, R. (2015). Shall we send humans to Holden Crater? How a geodesic GIS approach can aid the landing site selection for future missions to Mars. In *First landing site/exploration zone workshop for human missions to the surface of Mars* (pp. 1049). Houston, TX: Lunar and Planetary Institute. LPI Contribution No. 1879.

Osterloo, M. M., Anderson, F. S., Hamilton, V. E., & Hynek, B. M. (2010). Geologic context of proposed chloride-bearing materials on Mars. *Journal of Geophysical Research*, *115*, E10012. https://doi.org/10.1029/2010JE003613

Putzig, N. E. (2006). Thermal inertia and surface heterogeneity on Mars, (PhD thesis). Boulder, CO: University of Colorado.

Richardson, J. A., Bleacher, J. E., & Glaze, L. S. (2013). The volcanic history of Syria Planum, Mars. *Journal of Volcanology and Geothermal Research*, *252*, 1–13. https://doi.org/10.1016/j.jvolgeores.2012.11.007

Robbins, S. J., & Hynek, B. M. (2012). A new global database of Mars impact craters ≥1 km: 1. Database creation, properties, and parameters. *Journal of Geophysical Research*, *117*, E05004. https://doi.org/10.1029/2011JE003966

Rothrock, B., Kennedy, R., Cunningham, C., Papon, J., Heverly, M., & Ono, M. (2016). SPOC: Deep learning-based terrain classification for Mars Rover missions, in: AIAA SPACE 2016, American Institute of Aeronautics and Astronautics https://doi.org/10.2514/6.2016-5539

Serrano, N., & Seraji, H. (2007). Landing site selection using fuzzy rule-based reasoning. In *Proceedings 2007 IEEE International Conference on Robotics and Automation* (pp. 4899–4904). https://doi.org/10.1109/ROBOT.2007.364234

Sethian, J. A. (1996). A fast marching level set method for monotonically advancing fronts. *Proceedings of the National Academy of Sciences*, *93*(4), 1591–1595. https://doi.org/10.1073/pnas.93.4.1591

Sethian, J. (1999). Fast marching methods. *SIAM Review*, *41*(2), 199–235. https://doi.org/doi:10.1137/S0036144598347059

Smith, D., Neumann, G., Arvidson, R. E., Guinness, E. A., & Slavney, S. (2003). Mars global surveyor laser altimeter mission experiment gridded data record, NASA Planetary Data System, MGS-M-MOLA-5-MEGDR-L3-V1.0.

Summons, R. E., Amend, J. P., Bish, D., Buick, R., Cody, G. D., Des Marais, D. J., et al. (2011). Preservation of Martian organic and environmental records: Final report of the Mars Biosignature Working Group. *Astrobiology*, *11*(2), 157–181. https://doi.org/10.1089/ast.2010.0506

Tanaka, K. L., Skinner, J. A., Dohm, J. M., Irwin, R. P. III, Kolb, E. J., Fortezzo, C. M., et al. (2014). Geologic map of Mars. In *USGS Numbered Series 3292*. Reston, VA: Geological Survey.

Tanaka, K. L., Skinner, J. A., & Hare, T. M. (2005). Geologic map of the northern plains of Mars, USGS Numbered Series 2888, U.S. Geological Survey.

Thomas, K., Benjamin, R.-K., Fernando, P., Brian, G., Matthias, B., Jonathan, F., et al. (2016). Jupyter Notebooks—A publishing format for reproducible computational workflows. In F. Loizides & B. Schmidt (Eds.), *Positioning and Power in Academic Publishing: Players, Agents and Agendas* (pp. 87–90). Amsterdam, Netherlands: IOS Press. https://doi.org/10.3233/978-1-61499-649-1-87

Walt, S. v. d., Colbert, S. C., & Varoquaux, G. (2011). The NumPy array: A structure for efficient numerical computation. *Computing in Science Engineering*, *13*(2), 22–30. https://doi.org/10.1109/MCSE.2011.37

Wordsworth, R. D. (2016). The climate of early Mars. *Annual Review of Earth and Planetary Sciences*, *44*(1), 381–408. https://doi.org/10.1146/annurev-earth-060115-012355

Zadeh, L. A. (1965). Fuzzy sets. *Information and control*, *8*(3), 338–353. https://doi.org/10.1016/S0019-9958(65)90241-X

Zahnle, K. (2001). Decline and fall of the Martian empire. *Nature*, *412*(6843), 209–213. https://doi.org/10.1038/35084148